Nano Research

Open Access

Research Article

# Constructing high-biosecurity $MoS_2$-based anodes for rapid and efficient lithium storage

Yixin Wang[1,2], Ruxia Qiao[1,2], Xueying Zheng[3], Wangyan Wu[3], Hao Yang[3], Stephanie Ling Jie Lee[1,2], Jian Peng[1,2], Jinyu Rong[1,2], Wei Luo[3], and Sijie Lin[1,2] ✉

[1] *College of Environmental Science and Engineering, Biomedical Multidisciplinary Innovation Research Institute, Shanghai East Hospital, Tongji University, Shanghai 200092, China*
[2] *Key Laboratory of Yangtze River Water Environment, Shanghai Institute of Pollution Control and Ecological Security, Tongji University, Shanghai 200092, China*
[3] *Institute of New Energy for Vehicles, School of Materials Science and Engineering, Tongji University, Shanghai 201804, China*

**Cite this article:** *Nano Research*, **2025**, *18*, 94907186. https://doi.org/10.26599/NR.2025.94907186

**ABSTRACT:** Lithium-ion batteries that integrate electrochemical performance and safety considerations offer advantages to curb the reliance on fossil fuels while minimizing the potential environmental risks. Transition metal disulfides and metal oxides with high specific capacity are promising candidates as anodes for lithium storage. However, neither the layered structure of $MoS_2$ nor the powder form of $In_2O_3$ is ideal for battery prolonged applications. Herein, we demonstrated a low-toxicity anode designed with hollow fibers to regulate the $MoS_2$ contact surface, significantly reducing biotoxicity and enhancing $Li^+$ diffusion. Density functional theory (DFT) calculations revealed that the interactions among $MoS_2$, $In_2O_3$, and the hollow structure lowered the Li-ion migration energy barrier hence fastening the diffusion. Moreover, the $MoS_2$-containing fiber showed significantly decreased toxicity in zebrafish embryos compared to $MoS_2$ alone, demonstrating a proof-of-principle of integrating functional nanomaterials into flexible fiber structures to improve both electrochemical performance and safety.

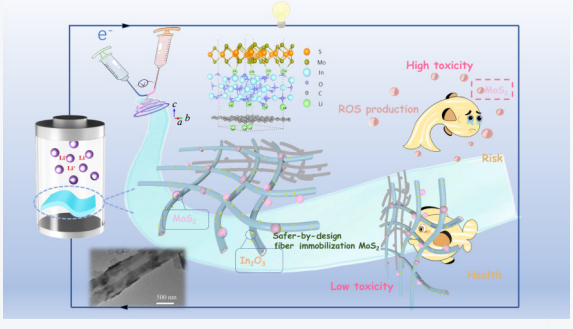


**KEYWORDS:** electrospun fibers, Li-ion battery, $MoS_2$, $In_2O_3$, hollow fiber, low-toxicity anode

## 1 Introduction

Lithium storage materials have garnered significant interest as a means to address the challenges of the global energy crisis [1–4]. Given the conventional graphite anodes' low capacity (370 mAh/g), demands for anode materials with good capacity and stability keep rising [5]. The advancement of nanotechnology has fostered the creation of nanomaterials with theoretical high capacity, such as zero-dimensional (0D) nanodots and two-dimensional (2D) transition metal disulfide (TMD) compounds. $MoS_2$ with graphite-like structures are ideal candidates for high-capacity batteries with a theoretical capacity of 670 mAh/g [6]. However, their layered structure tends to collapse during lithiation and de-lithiation cycling, resulting in significant deteriorations of battery performance [7–10]. Zero-dimensional metal oxide nanodots such as indium oxide also have the potential to serve as anode materials for high energy density lithium-ion batteries (LIBs) given their theoretical reversible capacity (500–1000 mAh/g) [11]. The nano-sized $In_2O_3$ could help preserve the structural integrity of the composite fiber when incorporated into the nanofiber matrix [12]. However, metal oxides alone exhibit low electrical conductivity and pulverization as anode materials. To address these challenges, integrating functional nanomaterials into a carbon (C) substrate could render structural support for $MoS_2$ while enhancing the overall electronic conductivity of the nanocomposites.

Electrospinning is a versatile method for preparing carbon nanofibers that integrate non-spinnable particles [13]. The incorporation of nanomaterials can offer an exceptionally robust framework support structure, effectively alleviating the volume expansion associated with the discharge/charging process [14–16]. To prevent cluster formation, which could result in structural damage, concentrations and particle sizes of 0D nanoparticles were the main characteristics to control when incorporated into fibers [17, 18]. In conventional electrospinning processes, nanodots are

**Received:** October 13, 2024; **Revised:** November 26, 2024
**Accepted:** December 12, 2024

✉Address correspondence to lin.sijie@tongji.edu.cn

often used to prepare fibers by mixing them with polymers through a single-fluid process [19]. The nanofibers' conductive network and hierarchical nanostructure can better control the electrochemical behavior of the nanodots [20]. In core–shell electrospinning, the size of the nanoparticles is closely related to the morphological characteristics, electrochemical performance, and distribution uniformity of the fiber shell layer [21]. For 2D nanosheets, such as $MoS_2$, the edge sites of the nanosheets are the main locations of active sites [21–23]. However, directly adding 2D nanosheets into the electrospinning fluid may hinder fluid mobility, reduce stability, and increase the risk of fiber breakage or structural irregularities. Therefore, it is beneficial to the overall performance by increasing the exposure of these edge sites while maintaining the structural stability of $MoS_2$. Moreover, electrospinning offers opportunities to manipulate the fiber structures, such as hollow nanostructures to create more space for lithium storage. The fiber structure also featured spatial buffering with active sites for enhanced capacity and stability [24, 25].

While significant advances have been made in the field of energy storage employing novel nanomaterials with high-performance value, their hazard potential has raised occupational and environmental health and safety concerns. $MoS_2$ has been shown to generate harmful reactive oxygen species (ROS) that cause oxidative damage to organisms [26, 27]. Zebrafish exposed to the suspension of $MoS_2$ developed pericardial edema, yolk sac edema, and tail malformations at 10 mg/L concentrations [28]. A recent study showed that the introduction of humic acid and fulvic acid into water containing $MoS_2$ nanosheets increased the zebrafish lethal concentration 50 (LC50), suggesting a mitigating effect on the toxicity of $MoS_2$ to zebrafish larvae [29]. Studies have also shown that by covering $MoS_2$ with extracellular polymeric substances (EPS) or natural organic matters (NOM), the toxicity in algae and zebrafish could be significantly reduced [30]. Therefore, it is possible to avoid the toxic effects by preventing a direct exposure of $MoS_2$ to living organisms [31, 32]. To apply safer-by-design for energy materials, the best practice would be to assess and avoid toxicity of the compositing materials at the designing phase [33–35].

Against this background, we set out to develop a hollow fiber that integrates $In_2O_3$ nanodots through electrospinning and $MoS_2$ through *in situ* synthesis. The electrochemical performance of the anodes composed of nanocomposite fibers was measured at a discharge capacity of 2276.0 mAh/g at 0.1 A/g and 1464 mAh/g in rate performance from 2.0 to 0.2 A/g. Density functional theory (DFT) calculations were conducted to simulate atomic interfacial structures and the adsorption sites and the reaction process was further validated by calculating the optimal positions and migration energy barriers of $Li^+$. Using zebrafish, the toxicity of the $MoS_2$ in powder form and $MoS_2$-containing anodes were compared. In comparison to the larval tail malformation and yolk sac edema induced by exposure to powdered $MoS_2$, the composite fiber had minimal impact on the growth and development of zebrafish embryos and larvae which demonstrates the successful implementation of a safer-by-design strategy.

## 2 Results and discussion

As depicted in Fig. 1(a), coaxial electrospinning was performed to fabricate a core–shell composite fiber with the shell composed of polyacrylonitrile (PAN) and $In_2O_3$ and the core composed of polyvinylpyrrolidone (PVP). Hydrothermally, $MoS_2$ was synthesized *in situ* after the prepared fibers were heat-treated in an Ar atmosphere to create hollow composite fibers. The resulting electrospun fibers appeared black with a highly flexible texture as shown in Fig. 1(b). Microscopically, the layered structure of $MoS_2$ decorated on the outer layer of the fibers, evidenced by scanning electron microscopy (SEM) (Figs. 1(c) and 1(d)). The outer diameter of the hollow fibers was approximately 465 ± 5 nm with an inner diameter of 120 ± 5 nm (Fig. 1(e)). Transmission electron microscopy (TEM) also confirmed the hollow structure of the In@HCF/$MoS_2$ (Fig. 1(f)) and clear lattice-spacing corresponding to $MoS_2$ could be seen under high-resolution TEM (Fig. 1(g)). The TEM image of In@HCF displayed a complete picture of the hollow condition of the fiber (Fig. S1 in the Electronic Supplementary Material (ESM)), with the shell layer containing $In_2O_3$ nanodots. Figure S2 in the ESM presents its full morphological characterizations. The constructed hollow composite fiber In@HCF/$MoS_2$ possessed a capillary behavior for faster absorption of liquid electrolyte, enabling rapid absorption of liquid electrolyte (Video S1 in the ESM) [36]. Overall, the electrospun fibers possessed a core/shell structure where the $In_2O_3$ nanodots were embedded in the inner layer and the layered $MoS_2$ was decorated on the outer layer. The hollow fibers containing different concentrations of $In_2O_3$ were used to determine the maximum capacity of the fiber shell layer (Table S1 in the ESM). When the concentrations of $In_2O_3$ reached 4%–8% (m/v) in the shell solution, spinning became impossible owing to the aggregation of $In_2O_3$. Thus, to maximize the presence of $In_2O_3$ in the fiber shell layer and ensure optimal cell capacity, the core–shell electrospun fibers can be efficiently produced by incorporating 1% (w/v ratio) $In_2O_3$, resulting in a smooth surface structure. Elemental mapping coupled with TEM was used to confirm the presence of C, In, Mo, and S (Fig. 1(h)). Clearly, C and In elements were evenly distributed in the structure, while Mo and S were concentrated in the shell layer of the hollow fiber. The presence of $MoS_2$ was also confirmed by the approximate ratio of Mo to S which is approximately 1:2.

To further study the surface characterizations of the In@HCF/$MoS_2$, X-ray photoelectron spectroscopy (XPS) and X-ray diffractometer (XRD) were carried out. The In@HCF/$MoS_2$ consisted of Mo, S and In, as shown in Fig. 2(a), which compares favorably to the SEM mapping pictures (Fig. 1(h)). The spectra of Mo 3d of In@HCF/$MoS_2$ (Fig. 2(b)) revealed typical $MoS_2$ peaks at 231.9 eV (Mo $3d_{3/2}$) and 228.8 eV (Mo $3d_{5/2}$) [37, 38]. S and In originated from $MoS_2$ and $In_2O_3$ in the In@HCF/$MoS_2$ (Figs. 2(c) and 2(d)), respectively [39, 40]. The splitting of S 2p into S $2p_{3/2}$ and S $2p_{1/2}$, which correspond to binding energies of 161.7 and 162.9 eV, respectively, indicates the presence of divalent sulfide ions ($S^{2-}$). Compared with In 3d spectra of $In_2O_3$, the binding energy of In@HCF/$MoS_2$ was shifted at 444.7 eV (In $3d_{5/2}$) and 452.3 eV (In $3d_{3/2}$). The results obtained by XRD (Fig. 2(e)) confirmed the crystalline structure of $MoS_2$ and $In_2O_3$. The position of the diffraction peak at 14.4° corresponded to the (002) crystal plane of $MoS_2$.

Charge density difference calculation was employed to aid the understanding of the interrelationship between the fiber's hollow structure and the lamellar structure of $MoS_2$. As depicted in Fig. 2(f), a three-dimensional model was used to demonstrate the charge density difference, consisting of top, middle, and bottom layers. The top layer was comprised of Mo and S atoms, representing $MoS_2$. The middle layer was comprised of In and O atoms, representing $In_2O_3$. The bottom layer contains C atoms, symbolizing carbon fibers. The quantum mechanical *ab initio* molecular code DMol3

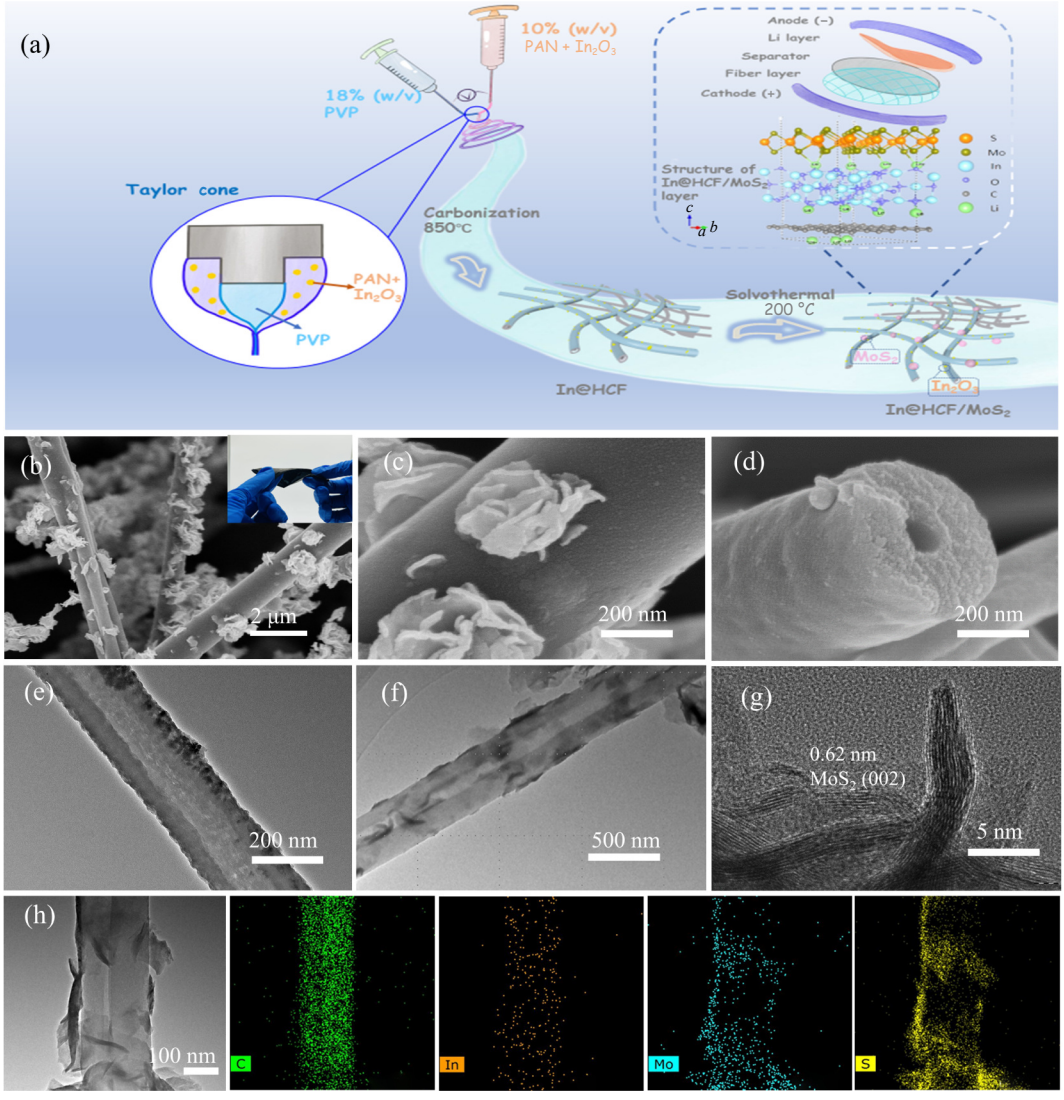


**Figure 1** Fabrication and characterizations of In@HCF/$MoS_2$. (a) Schematic diagram illustrating the overall process of the fabrication of In@HCF/$MoS_2$ fibers through coaxial electrospinning. (b) Photograph of In@HCF/$MoS_2$. (c) Representative SEM images of In@HCF/$MoS_2$. (d) Close-up SEM images showing the presence of layered structure on the outer layer of the electrospun fibers. (e) SEM image of the cross-section of In@HCF/$MoS_2$. (f) Representative TEM images of In@HCF/$MoS_2$. (g) High-resolution TEM image of In@HCF/$MoS_2$ showing the typical [002] lattice spacing (0.62 nm) corresponding to $MoS_2$. (h) Elemental mapping of a typical TEM image of In@HCF/$MoS_2$, showing the distribution of C, In, Mo, and S elements with the electrospun fiber.

was used to calculate the experiment's transition states as well as its optimized structure. The blue region represents electron depletion and the purple region represents electron accumulation, revealing the interaction of electrons in the overall structure of In@HCF/$MoS_2$. At the interface between the hollow carbon fibers and $In_2O_3$, a small amount of charge was transferred from C atoms to O atoms near $In_2O_3$. This charge transfer caused the Li atom adsorption site to be offset towards $In_2O_3$. Moreover, there was minimal charge transfer at the interface between $In_2O_3$ and $MoS_2$. The interaction between $In_2O_3$ and $MoS_2$ did influence the distribution of charge of $MoS_2$, as depicted by the blue region of the interaction between $In_2O_3$ and $MoS_2$ in the figure which was consistent with the XPS data. This effect resulted in a shift of the Li adsorption site towards $In_2O_3$. Owing to the weak contact between the $In_2O_3$ and $MoS_2$, migration channels might emerge at the interface, thereby providing sufficient sites for Li atom adsorption.

Electrochemical tests were conducted to assess the energy storage characteristics of the In@HCF/$MoS_2$, In@HCF, and HCF electrodes for use in LIBs applications. In@HCF/$MoS_2$, In@HCF, and HCF electrodes and lithium foil were assembled into a CR2025 coin-type battery to evaluate the properties. The charge and discharge performance of the three electrodes were compared during the 1st, 2nd, and 3rd cycles, within a voltage range of 0.01–3 V and at a current density of 0.1 A/g (Fig. 3(a) and Fig. S3 in the ESM). The initial Coulombic efficiency (ICE) for In@HCF/$MoS_2$ is ~ 80% and a discharge capacity of 2276.0 mAh/g is delivered in the first cycle. The charge and discharge profiles overlapped after solid electrolyte interphase (SEI) in the initial cycle. HCF and In@HCF exhibited electrochemical performance (406.2 and 1301.3 mAh/g) during the first three turns of charge/discharge (Figs. S3(a) and S3(b) in the ESM). When comparing In@HCF/$MoS_2$ to In@HCF and HCF, the performance difference is substantial.

Combined with cyclic voltammetry (CV) curves, the electrochemical processes happening in In@HCF/$MoS_2$ LIBs were investigated (Fig. 3(b)). In the discharge cycle, the cathodic peak at 0.3 V should be attributed to the gradual formation of $Li_xIn$ alloy

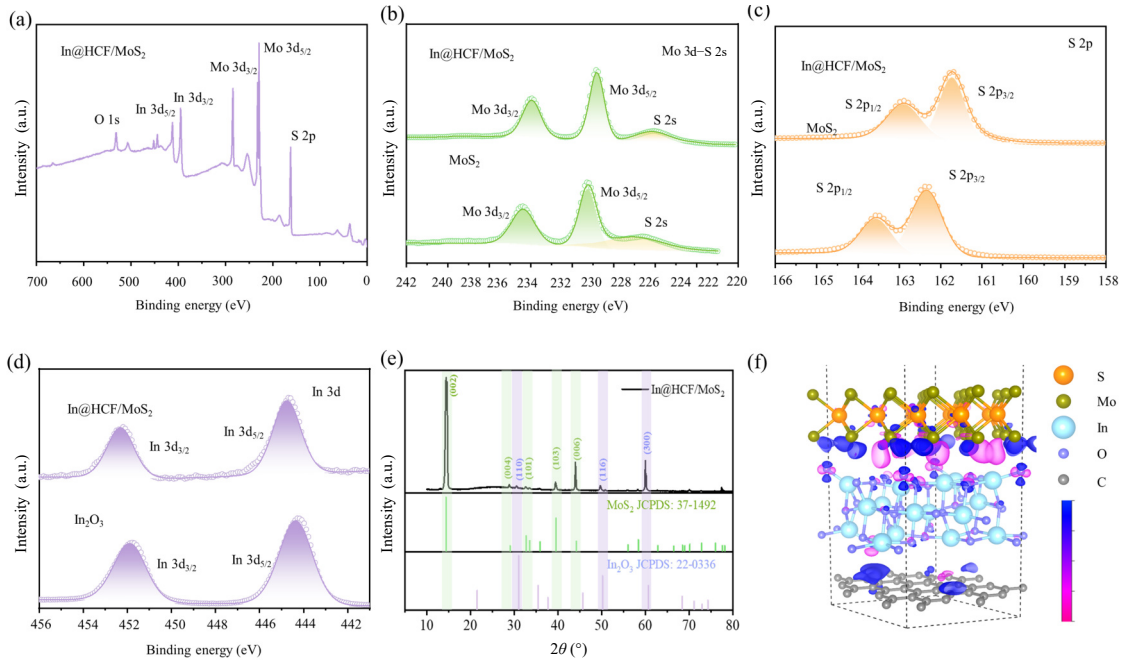


**Figure 2** The diffractogram and charge density difference diagram of In@HCF/$MoS_2$. (a) XPS survey spectrum of In@HCF/$MoS_2$. XPS spectra of (b) Mo 3d–S 2s, (c) S 2p, and (d) In 3d for In@HCF/$MoS_2$, $MoS_2$, and $In_2O_3$. (e) XRD pattern of the In@HCF/$MoS_2$. (f) Differential charge density of In@HCF/$MoS_2$ interface, where the blue and purple regions indicate the negative and positive charges of electrons, respectively.

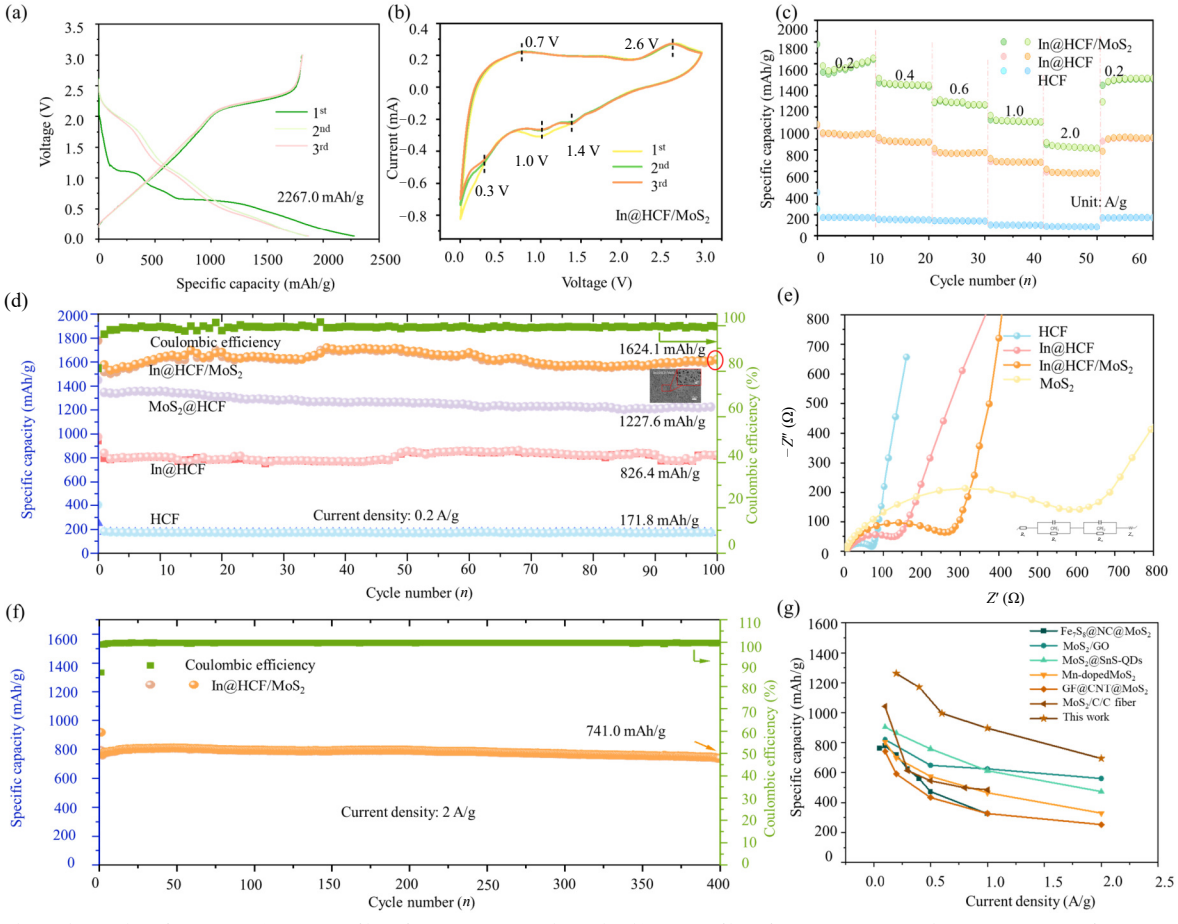


**Figure 3** Electrochemical performance. (a) GCD profiles of In@HCF/$MoS_2$ electrode. (b) CV profiles of In@HCF/$MoS_2$ with a scanning rate of 0.05 mV/s. (c) Rate capabilities. (d) Cycling performance and Coulombic efficiency of In@HCF/$MoS_2$, In@HCF, and HCF electrodes at the current density of 0.2 A/g. Inset corresponds to SEM images of In@HCF/$MoS_2$ electrode after 100 cycles. (e) Nyquist plots of In@HCF/$MoS_2$, In@HCF, HCF, and $MoS_2$ electrodes before cycling. (f) Long cycling performance and Coulombic efficiency of In@HCF/$MoS_2$ electrodes at 2 A/g for cycling stability. (g) Comparisons of rate capability between In@HCF/$MoS_2$ and other materials.

during lithium insertion. The reduction peak at 1.4 V indicates the formation of $Li_xMoS_2$ ($MoS_2 + xLi^+ + xe \rightarrow Li_xMoS_2$), which belongs to the intercalation reaction formed by the insertion of $Li^+$ into $MoS_2$. The peak at 1.0 V is the one-step conversion of $Li_x$ $MoS_2$ to produce Mo and $2Li_2S$ ($LiMoS_2 + (4 - x)Li^+ + (4 - x)e^- \rightarrow Mo + 2Li_2S$) [41]. The initial scan curve of In@HCF/$MoS_2$ mostly overlaps with the subsequent one, indicating the outstanding reversibility and high stability of the pole piece. The reduction peak appearing at 2.6 V is thought to be the generation of $Li_2S$ and the conversion of Mo to $MoS_2$ [10, 12, 42]. In the following scans, the CV curves gradually stabilized and nearly converged. The anodic peak at 0.7 V is due to lithium/indium dealloying during charging. The findings indicate that the In@HCF/$MoS_2$ electrode demonstrates outstanding cycling stability during the discharge/charge process.

Further assessment was conducted to assess the rate capability of the In@HCF/$MoS_2$ electrode. The rate performances of the In@HCF/$MoS_2$ electrode were examined at different current densities from 0.2 to 2 A/g (Fig. 3(c)). Although both the In@HCF/$MoS_2$ electrode, HCF electrode, and the In@HCF electrode have a generally similar discharge capacity when forming cycles, the systems exhibited a capacity discrepancy. At 0.2, 0.4, 0.6, 1.0, and 2.0 A/g, the In@HCF produces a rapidly fading discharge capacity of 957.1, 913.0, 812.2 and 720.0 mAh/g. The value corresponding to the In@HCF/$MoS_2$ electrode is enhanced to 1579.2, 1462.8, 1243.1, 1119.9, and 866.9 mAh/g. After 50 cycles of charge/discharge tests at different current densities, the high specific capacity is still maintained when the current density returns to the initial 0.2 A/g. The inclusion of a hollow fiber structure containing $In_2O_3$ and $MoS_2$ sheet layer in the electrode design results in increased structural stability during the charging and discharging processes. This shorter diffusion path for $Li^+$ contributed to the high specific capacity and cycle stability, as demonstrated by maintaining stable performance even after switching between high and low current densities for 10 cycles [43]. Figure 3(d) illustrates the cycling stability of HCF, In@HCF, $MoS_2$@HCF, and In@HCF/$MoS_2$ electrodes, tested at a current density of 0.2 A/g. HCF, In@HCF, $MoS_2$@HCF, and In@HCF/$MoS_2$ electrodes retained capacities at 171.8, 826.4, 1227.6, and 1624.1 mAh/g, respectively. The mixture of In@HCF and $MoS_2$ showed undesired reducing capacities (Figs. S4 in the ESM). To further examine the impact of In@HCF/$MoS_2$ fibers on reducing $MoS_2$'s volumetric swelling, we used SEM to analyze the morphology of fiber electrodes and $MoS_2$-coated electrodes on copper foil after cycling. Consistency was ensured by taking multiple measurements across various electrode locations. After 100 cycles (Fig. S5 in the ESM and inset of Fig. 3(d)), SEM images revealed deeper surface cracks on the $MoS_2$-coated electrode, whereas the In@HCF/$MoS_2$ electrode maintained intact surface.

The presence of $MoS_2$ in the composite fiber facilitated the storage of $Li^+$ through a unique insertion pathway, thanks to its layered S–Mo–S intercalation structure and numerous active sulfur sites. Pure $MoS_2$ has low structural stability and exhibits poor electrochemical capabilities (Fig. 3(e) and Table S2 in the ESM). In the Nyquist diagram, the resistance of SEI ($R_f$) may produce a high-frequency semicircle, the interfacial charge transfer resistance of electrode and electrolyte, electrode reaction ($R_{ct}$) exists in the middle-frequency region, and the $Li^+$ diffusion process impedance (Warburg impedance) ($Z_w$) exists in the low-frequency region. The charge transfer resistance of 211.8 Ω is seen in the electrochemical impedance spectroscopy (EIS) of In@HCF/$MoS_2$, which is less than the 569.3 Ω of $MoS_2$. The charge transfer resistance values for In@HCF and HCF are 132 and 68.2 Ω, respectively. This observation suggests a direct synergistic effect resulting from the combination of the composite fiber In@HCF with $MoS_2$. The surface between $In_2O_3$ and $MoS_2$ in the fiber shell layer played a favorable role in Li storage. By attaching $MoS_2$ to the exterior of the fiber, Ostwald ripening, a phenomenon where larger particles grow at the expense of smaller ones, was prevented [44, 45].

Both the HCF and the In@HCF show consistent long-term cycling performance, and the utilization of $In_2O_3$ in the In@HCF can enhance the specific capacity of the overall battery. The discharge capacity of the In@HCF/$MoS_2$ electrode can be stabilized by cycling for 400 cycles at 2.0 A/g holding a capacity retention of 81.1% (Fig. 3(f)). In comparison to the existing research on the individual lithium storage capacity of $MoS_2$, In@HCF/$MoS_2$ demonstrates structural and capacity advantages [46–48]. The mechanical characteristics of the hollow fiber effectively suppressed the volume expansion and contraction of $MoS_2$ during cycling, contributing to the stability of batteries and prolonged cycling life. These findings highlighted the superior electrochemical performance of the In@HCF/$MoS_2$ electrode, including high specific capacity, reversibility, and rate capability. Hollow carbon fibers provide a robust framework that supports $MoS_2$, preventing it from collapsing. This support is crucial during the repeated lithiation and delithiation processes, which typically cause volume changes and structural degradation in $MoS_2$. The carbon fibers help maintain the structural integrity of the electrode, reducing the mechanical stress and strain that $MoS_2$ experiences during cycling. The hollow carbon fibers mitigate the pulverization of $MoS_2$ particles, which is a common issue due to the significant volume expansion and contraction. This reduction in pulverization leads to a more stable electrochemical performance over many cycles. The presence of carbon fibers ensures a more uniform distribution of lithium ions within the electrode material, which helps in maintaining consistent electrochemical reactions. The unique design incorporating a hollow fiber structure with $In_2O_3$ and $MoS_2$ provided enhanced properties for lithium-ion battery applications. The In@HCF/$MoS_2$ presented here exhibits a significantly higher reversible capacity at high current densities compared to previously reported results (Fig. 3(g) and Tables S4 and S5 in the ESM).

DFT simulations were performed for the migration diffusion of Li at different interfaces to investigate the rate properties of the material. The In@HCF and In@HCF/$MoS_2$ structures (Models I and II) were constructed, where the structural size of the hollow fibers was a $2 \times 3^{1/2} \times 2 \times 3^{1/2} \times 1$ supercell and the structural size of the $MoS_2$ was a $7^{1/2} \times 7^{1/2} \times 1$ supercell. The energy-stabilized adsorption sites of Li ions in Models I and II are calculated (Figs. 4(a)–4(e)), and side and top views of different interfaces of the lithium adsorption sites are observed (Figs. S6–S8 in the ESM), to identify the favorable diffusion pathways. The special folded structure of $In_2O_3$ leads to a close distance between Li and O, which has strong adsorption properties for Li ions. The migration diffusion paths are determined by the stable adsorption sites of Li which in both Models I and II were shifted toward $In_2O_3$. The binding energy ($E_b$) of Li is based on the energy of Models I or II Li embedded in the whole system ($E_{total}$) minus the energy of Models I or II interface ($E_{interface}$) and the energy of single Li ($E_{Li}$). The equation is $E_b = E_{total} - E_{interface} - E_{Li}$. The information on the binding energy of Li at different adsorption sites was shown in

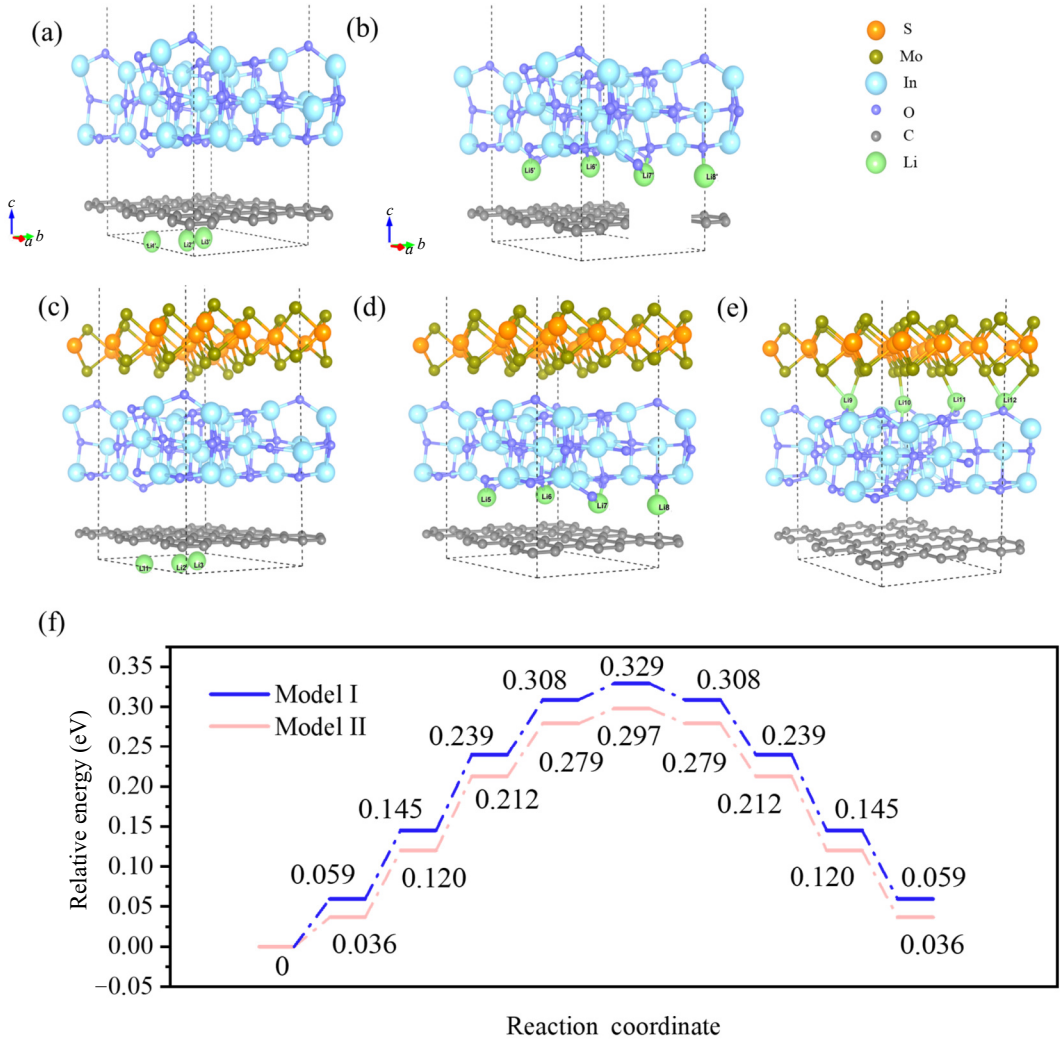


**Figure 4** The sites of Li and its diffusion energy distribution. (a) Inside the hollow fiber of In@HCF. (b) Interface between hollow fibers and $In_2O_3$ of In@HCF. (c) Inside the hollow fiber of In@HCF/$MoS_2$. (d) Interface between hollow fibers and $In_2O_3$ of In@HCF/$MoS_2$. (e) The interface between $In_2O_3$ and $MoS_2$ of In@HCF/$MoS_2$. (f) Diffusion energy distribution of Li at the In@HCF and In@HCF/$MoS_2$ interfaces.

Table S3 in the ESM, where the negative values represented mutual attraction and the smaller values of binding energy indicated stronger adsorption. Based on the binding energy calculations, the optimal adsorption paths of Models I and II are inside the hollow fibers, and the migration direction and motion trajectory of lithium ions are shown in Fig. S9 and Video S2 in the ESM [49]. The climbing image nudged elastic band (CL-NEB) method is used to calculate the energy of Li at different sites along the diffusion path to obtain the migration potential barrier. Figure 4(f) shows the migration potential barriers of Li along the best diffusion path in Models I and II. The migration energy barrier is lower, which means that Li diffuses faster in the system. The migration energy barrier of Model II at this diffusion condition 0.261 eV is lower than that of Model I 0.27 eV. As a result, DFT calculations supported the hypothesis that the accelerated movement of lithium ions in Model II contributed to the overall improvement in the batteries' performance during the reaction.

Toxicity assessment using zebrafish was conducted to investigate the toxicity potential of the composite fibers that were developed. The purpose of the study was to ascertain if immobilizing In@HCF/$MoS_2$, which was created following the safer-by-design principle, could lessen the harmful effects of $MoS_2$-induced reactive oxygen species on living organisms. Healthy zebrafish embryos were exposed to the nanoparticles and nanofibers in Holtfreter's medium (Fig. 5(a)). To assess the toxicity potential of $MoS_2$ and $In_2O_3$ (in the shell of fiber), waterborne exposure experiments were conducted using different concentrations of $MoS_2$ (10, 20, and 40 ppm) and $In_2O_3$ (10 to 100 ppm). Meanwhile, the In@HCF/$MoS_2$ electrode was used to verify the developmental effects of composite fibers on zebrafish embryos (Fig. 5(b)). Exposure to $MoS_2$ nanosheets led to decreased embryo hatching rates and increased larval malformation rates (Figs. 5(c) and 5(d)). Although $MoS_2$ did not cause embryo mortality, tail malformation and yolk sac edema were among the malformations typically observed (Fig. 5(d)). In contrast, $In_2O_3$ exposure was performed over a wide range of concentrations (10, 50 and 100 ppm). which did not affect zebrafish embryo survival, mortality, or malformation rates (Fig. S10 in the ESM). Interestingly, the In@HCF/$MoS_2$ demonstrated negligible harmful effects on zebrafish larvae, as In@HCF/$MoS_2$-exposed zebrafish larvae exhibited normal development (Figs. 5(c) and 5(d)). The degree of toxicity and the properties of nanomaterials are influenced by various factors, including their size,

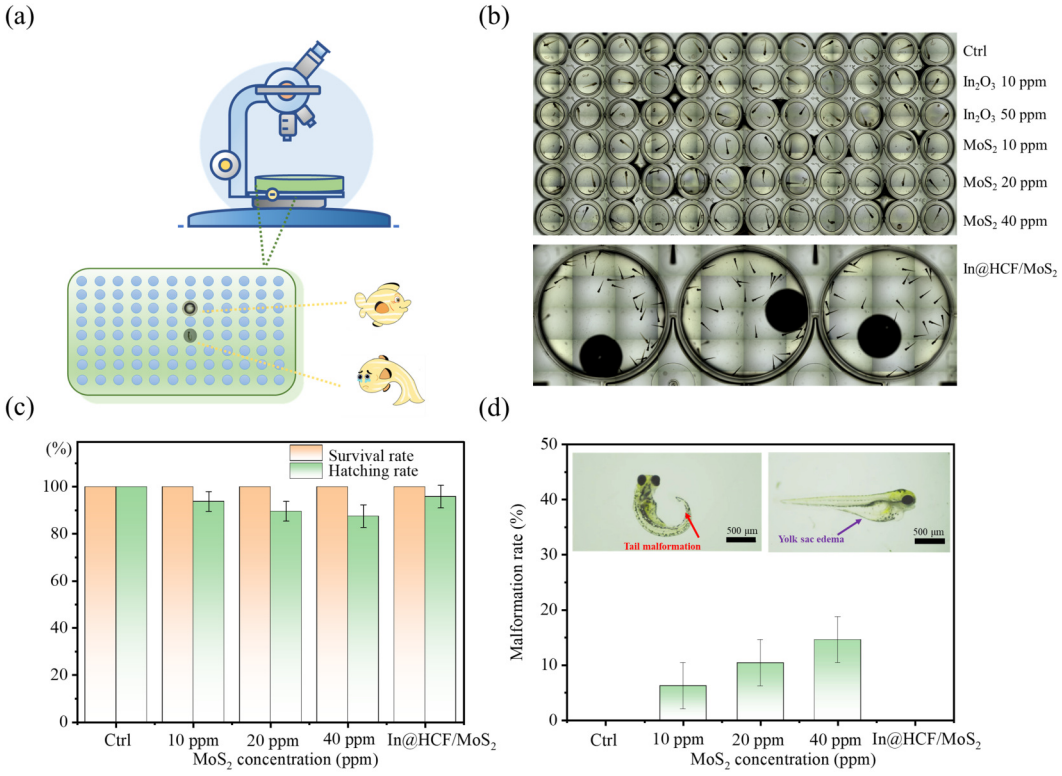


**Figure 5** Toxicity assessment of $In_2O_3$, $MoS_2$, and In@HCF/$MoS_2$ using zebrafish embryos and larvae. (a) Schematic diagram depicting the toxicity screening methodology for zebrafish embryos. 2 h post fertilization zebrafish embryos were rinsed and placed in Petri dishes. Healthy embryos were individually selected and manually transferred into 96-well and 6-well clear bottom culture plates. Zebrafish embryos were exposed to suspensions of $In_2O_3$, $MoS_2$, and In@HCF/$MoS_2$ from 4 h post fertilization to 5 days post fertilization in different concentration. Visual observation of death, hatching, and morphological abnormalities was captured for each well using the EVOS intelligent cell imaging system. (b) Images of zebrafish embryos exposed to different concentrations of $In_2O_3$ and $MoS_2$, as well as In@HCF/$MoS_2$ suspensions at 120 h. The first row comprises the control group of embryos. (c) Hatching rate and survival rate of toxicity in zebrafish embryos and larvae induced by $MoS_2$ and In@HCF/$MoS_2$. (d) Digital photos showing the typical malformation of the hatched larvae after exposure to $MoS_2$ and In@HCF/$MoS_2$.

shape, composition, surface charge, and functionalization [50]. Utilizing electrospun nanofibers as a framework structure, $MoS_2$ nanosheets are able to grow proximate to the fiber wall, thereby preventing direct interaction with the zebrafish embryonic chorion. The large mesh structure of the fiber immobilized $MoS_2$ and attenuated the direct interaction with the chorion. Therefore, the developed In@HCF/$MoS_2$ significantly reduced the toxicity potential of $MoS_2$, minimizing potential exposure risks and ensuring the safety and well-being of staff in occupational settings.

## 3 Conclusions

In@HCF/$MoS_2$ electrode was successfully fabricated by *in situ* synthesis of $MoS_2$ nanosheets in the hollow fiber surface layer. Benefiting from the composite hollow skeleton structure, the damage of the $MoS_2$ during long cycling was successfully prevented. Extensive characterizations and DFT calculations elaborated that In@HCF/$MoS_2$ exhibited enhanced electrochemical stability and rate performance as an anode material. Meanwhile, the hollow skeleton structure containing $In_2O_3$ was effective in lowering $MoS_2$, minimizing the environmental risk. By integrating a safer-by-design strategy with the concept of reducing toxicity potential in the design of flexible energy storage materials, this study offers a promising approach to the environmentally friendly design of energy materials. The findings of this research pave the way for the development of green high-capacity fiber batteries with improved performance and reduced environmental impact.

**Electronic Supplementary Material**: Supplementary material (detail experimental method, characterization method, computational methods, TEM image of In@HCF, SEM image and TEM image of $In_2O_3$, galvanostatic charge–discharge (GCD) profiles of HCF and In@HCF at 0.1 A/g, GCD profiles at 0.2 A/g between the In@HCF/$MoS_2$, In@HCF and HCF electrodes, different view of hollow fibers, In@HCF and In@HCF/$MoS_2$, top view of diffusion paths in hollow fiber, zebrafish embryos exposed to suspensions of different $In_2O_3$ concentrations at 24 h, and table of electrospinning parameters of core–shell fibers, table of Nyquist plot equivalent circuit fitting the corresponding resistance values, table of binding energy ($E_b$) and charge transfer ($q$) of In@HCF and In@HCF/$MoS_2$ and table of comparison of electrochemical rate performance of the LIBs of $MoS_2$ anode) is available in the online version of this article at https://doi.org/10.26599/NR.2025.94907186.

## Data availability

All data needed to support the conclusions in the paper are presented in the manuscript and the Electronic Supplementary Material. Additional data related to this paper may be requested from the corresponding author upon request.

## Acknowledgements

This work was financially supported by the National Natural

Science Foundation of China (No. 22176150) and the Fundamental Research Funds for the Central Universities.

## Declaration of competing interest

All the contributing authors report no conflict of interests in this work.

## Author contribution statement

Y. X. W.: Data curation, writing – original draft, investigation. R. X. Q.: Formal analysis, investigation. X. Y. Z., W. Y. W., H. Y., S. L. J. L., J. P., and J. Y. R.: Formal analysis. W. L.: Comments to manuscript. S. J. L.: Conceptualization, project administration, writing, funding acquisition, writing – review & editing. All the authors have approved the final manuscript.

## Informed consent

Not applicable.

## Ethics statement

The animal study protocol was approved by the Institutional Animal Care and Use Committee at Tongji University (Protocol No. TJAD00422B01).

## Use of AI statement

None.

## References

[1] Kang, Q.; Li, Y.; Zhuang, Z. C.; Yang, H. J.; Luo, L. X.; Xu, J.; Wang, J.; Guan, Q. H.; Zhu, H.; Zuo, Y. Z. et al. Engineering a dynamic solvent-phobic liquid electrolyte interphase for long-life lithium metal batteries. *Adv. Mater.* **2024**, *36*, 2300799.

[2] Liu, Y. L.; Zhuang, Z. C.; Liu, Y. X.; Liu, N. Y.; Li, Y. X.; Cheng, Y. Y.; Yu, J. W.; Yu, R. H.; Wang, D. S.; Li, H. T. Shear-strained Pd single-atom electrocatalysts for nitrate reduction to ammonia. *Angew. Chem., Int. Ed.* **2024**, *63*, e202411396.

[3] Hu, B.; Xu, J.; Fan, Z. J.; Xu, C.; Han, S. C.; Zhang, J. X.; Ma, L. B.; Ding, B.; Zhuang, Z. C.; Kang, Q. et al. Covalent organic framework based lithium-sulfur batteries: Materials, interfaces, and solid-state electrolytes. *Adv. Energy Mater.* **2023**, *13*, 2203540.

[4] Kang, Q.; Li, Y.; Zhuang, Z. C.; Wang, D. S.; Zhi, C. Y.; Jiang, P. K.; Huang, X. Y. Dielectric polymer based electrolytes for high-performance all-solid-state lithium metal batteries. *J. Energy Chem.* **2022**, *69*, 194–204.

[5] Kong, X. L.; Zhao, X. H.; Li, C.; Jia, Z. M.; Yang, C. K.; Wu, Z. Y.; Zhao, X. D.; Zhao, Y.; He, F.; Ren, Y. M. et al. Terminal group-oriented self-assembly to controllably synthesize a layer-by-layer $SnSe_2$ and MXene heterostructure for ultrastable lithium storage. *Small* **2023**, *19*, 2206563.

[6] Yu, W. J.; Cui, B. T.; Han, J. M.; Zhu, S. S.; Xu, X. H.; Tan, J. X.; Xu, Q. J.; Min, Y. L.; Peng, Y. T.; Liu, H. M. et al. *In situ* encapsulation of $SnS_2$/$MoS_2$ heterojunctions by amphiphilic graphene for high-energy and ultrastable lithium-ion anodes. *Adv. Sci.* **2024**, *11*, 2405135.

[7] Yu, H. X.; Pan, J. N.; Zhang, Y. X.; Wang, L. L.; Ji, H. C.; Xu, K. Y.; Zhi, T.; Zhuang, Z. C. Designing multi-heterogeneous interfaces of Ni-$MoS_2$@$NiS_2$@$Ni_3S_2$ hybrid for hydrogen evolution. *Nano Res.* **2024**, *17*, 4782–4789.

[8] Yu, H. X.; Pan, J. N.; Chen, K.; Chao, W.; Zhuang, Z. C.; Feng, S. Z.; Chen, J. M.; Xie, L, B.; Wang, L. L.; Zhao, Q. $MoS_x$ nanowire networks derived from $[Mo_3S_{13}]^{2-}$ clusters for efficient electrocatalytic hydrogen evolution. *Nano Res.* **2024**, *17*, 6910–6915.

[9] Li, S. W.; Liu, Y. C.; Zhao, X. D.; Shen, Q. Y.; Zhao, W.; Tan, Q. W.; Zhang, N.; Li, P.; Jiao, L. F.; Qu, X. H. Sandwich-like heterostructures of $MoS_2$/graphene with enlarged interlayer spacing and enhanced hydrophilicity as high-performance cathodes for aqueous zinc-ion batteries. *Adv. Mater.* **2021**, *33*, 2007480.

[10] Zhuang, Z. C.; Xia, L. X.; Huang, J. Z.; Zhu, P.; Li, Y.; Ye, C. L.; Xia, M. G.; Yu, R. H.; Lang, Z. Q.; Zhu, J. X. et al. Continuous modulation of electrocatalytic oxygen reduction activities of single-atom catalysts through p-n junction rectification. *Angew. Chem., Int. Ed.* **2023**, *62*, e202212335.

[11] Zhu, J.; Chen, L. B.; Xu, Z.; Lu, B. G. Electrospinning preparation of ultra-long aligned nanofibers thin films for high performance fully flexible lithium-ion batteries. *Nano Energy* **2015**, *12*, 339–346.

[12] Xu, H. J.; Wang, L.; Zhong, J.; Wang, T.; Cao, J. H.; Wang, Y. Y.; Li, X. Q.; Fei, H. L.; Zhu, J.; Duan, X. D. Ultra-stable and high-rate lithium ion batteries based on metal-organic framework-derived $In_2O_3$ nanocrystals/hierarchically porous nitrogen-doped carbon anode. *Energy Environ. Mater.* **2020**, *3*, 177–185.

[13] Chen, Z. L.; Wu, R. B.; Wang, H.; Zhang, K. H. L.; Song, Y.; Wu, F. L.; Fang, F.; Sun, D. L. Embedding ZnSe nanodots in nitrogen-doped hollow carbon architectures for superior lithium storage. *Nano Res.* **2018**, *11*, 966–978.

[14] Liu, Y. C.; Wang, F. F.; Fan, L. Z. Self-standing Na-storage anode of $Fe_2O_3$ nanodots encapsulated in porous N-doped carbon nanofibers with ultra-high cyclic stability. *Nano Res.* **2018**, *11*, 4026–4037.

[15] Kang, Q.; Zhuang, Z. C.; Liu, Y. J.; Liu, Z. H.; Li, Y.; Sun, B.; Pei, F.; Zhu, H.; Li, H. F.; Li, P. L. et al. Engineering the structural uniformity of gel polymer electrolytes via pattern-guided alignment for durable, safe solid-state lithium metal batteries. *Adv. Mater.* **2023**, *35*, 2303460.

[16] Kang, Q.; Zhuang, Z. C.; Li, Y.; Zuo, Y. Z.; Wang, J.; Liu, Y. J.; Shi, C. Q.; Chen, J.; Li, H. F.; Jiang, P. K. et al. Manipulating dielectric property of polymer coatings toward high-retention-rate lithium metal full batteries under harsh critical conditions. *Nano Res.* **2023**, *16*, 9240–9249.

[17] Choi, J. M.; Saroha, R.; Kim, J. S.; Jang, M. R.; Cho, J. S. Porous nanofibers comprising VN nanodots and densified N-doped CNTs as redox-active interlayers for Li–S batteries. *J. Power Sources* **2023**, *559*, 232632.

[18] Li, Z.; Zhang, C. Y.; Bu, J. T.; Zhang, L.; Cheng, L. L.; Wu, M. H. Constructing a novel carbon skeleton to anchor Sn/$SnO_2$ nanodots for flexible supercapacitor with excellent rate capability. *Carbon* **2022**, *194*, 197–206.

[19] Wu, Y.; Wei, Z. X.; Xu, R.; Gong, Y.; Gu, L.; Ma, J. M.; Yu, Y. Boosting the rate capability of multichannel porous $TiO_2$ nanofibers with well-dispersed Cu nanodots and $Cu^{2+}$-doping derived oxygen vacancies for sodium-ion batteries. *Nano Res.* **2019**, *12*, 2211–2217.

[20] Li, Q. H.; Zhang, W.; Peng, J.; Yu, D. D.; Liang, Z. X.; Zhang, W.; Wu, J. W.; Wang, G. Y.; Li, H. X.; Huang, S. M. Nanodot-in-nanofiber structured carbon-confined $Sb_2Se_3$ crystallites for fast and durable sodium storage. *Adv. Funct. Mater.* **2022**, *32*, 2112776.

[21] Lian, X. T.; Xu, N.; Ma, Y. C.; Hu, F.; Wei, H. X.; Chen, H. Y.; Wu, Y. Z.; Li, L. L.; Li, D. S.; Peng, S. J. *In-situ* formation of $Co_{1-x}S$ hollow polyhedrons anchored on multichannel carbon nanofibers as self-supporting anode for lithium/sodium-ion batteries. *Chem. Eng. J.* **2021**, *421*, 127755.

[22] Zhang, C. L.; Jiang, Z. H.; Lu, B. R.; Liu, J. T.; Cao, F. H.; Li, H.; Yu, Z. L.; Yu, S. H. $MoS_2$ nanoplates assembled on electrospun polyacrylonitrile-metal organic framework-derived carbon fibers for lithium storage. *Nano Energy* **2019**, *61*, 104–110.

[23] Jiang, H.; Ren, D. Y.; Wang, H. F.; Hu, Y. J.; Guo, S. J.; Yuan, H. Y.; Hu, P. J.; Zhang, L.; Li, C. Z. 2D monolayer $MoS_2$-carbon

interoverlapped superstructure: Engineering ideal atomic interface for lithium ion storage. *Adv. Mater.* **2015**, *27*, 3687–3695

[24] Zhang, C. L.; Yu, S. H. Nanoparticles meet electrospinning: Recent advances and future prospects. *Chem. Soc. Rev.* **2014**, *43*, 4423–4448.

[25] Cao, X. W.; Ma, C.; Luo, L.; Chen, L.; Cheng, H.; Orenstein, R. S.; Zhang, X. W. Nanofiber materials for lithium-ion batteries. *Adv. Fiber Mater.* **2023**, *5*, 1141–1197.

[26] Zhang, Y.; Srot, V.; Moudrakovski, I.; Feng, Y. Z.; van Aken, P. A.; Maier, J.; Yu, Y. Boosting sodium storage in $TiF_3$/carbon core/sheath nanofibers through an efficient mixed-conducting network. *Adv. Energy Mater.* **2019**, *9*, 1901470.

[27] Nel, A.; Xia, T.; Mädler, L.; Li, N. Toxic potential of materials at the nanolevel. *Science.* **2006**, *311*, 622–627.

[28] Zou, W.; Wan, Z. P.; Zhao, C. X.; Zhang, G. Q.; Zhang, X. L.; Zhou, Q. X. Impact of algal extracellular polymeric substances on the environmental fate and risk of molybdenum disulfide in aqueous media. *Water Res.* **2021**, *205*, 117708.

[29] Zou, W.; Ma, S.; Ma, H. W.; Zhang, G. Q.; Cao, Z. G.; Zhang, X. L. Componential and molecular-weight-dependent effects of natural organic matter on the colloidal behavior, transformation, and toxicity of $MoS_2$ nanoflakes. *J. Hazard. Mater.* **2023**, *459*, 132186.

[30] Wang, Z. Y.; von dem Bussche, A.; Qiu, Y.; Valentin, T. M.; Gion, K.; Kane, A. B.; Hurt, R. H. Chemical dissolution pathways of $MoS_2$ nanosheets in biological and environmental media. *Environ. Sci. Technol.* **2016**, *50*, 7208–7217.

[31] Hao, J. L.; Song, G. S.; Liu, T.; Yi, X.; Yang, K.; Cheng, L.; Liu, Z. *In vivo* long-term biodistribution, excretion, and toxicology of pegylated transition-metal dichalcogenides $MS_2$ (m = Mo, W, Ti) nanosheets. *Adv. Sci.* **2017**, *4*, 1600160.

[32] Shang, E. X.; Li, Y.; Niu, J. F.; Zhou, Y. J.; Wang, T. Y.; Crittenden, J. C. Relative importance of humic and fulvic acid on ROS generation, dissolution, and toxicity of sulfide nanoparticles. *Water Res.* **2017**, *124*, 595–604.

[33] Lin, S. J.; Yu, T. Y.; Yu, Z. Y.; Hu, X. L.; Yin, D. Q. Nanomaterials safer-by-design: An environmental safety perspective. *Adv. Mater.* **2018**, *30*, 1705691.

[34] Hussain, S. M.; Braydich-Stolle, L. K.; Schrand, A. M.; Murdock, R. C.; Yu, K. O.; Mattie, D. M.; Schlager, J. J.; Terrones, M. Toxicity evaluation for safe use of nanomaterials: Recent achievements and technical challenges. *Adv. Mater.* **2009**, *21*, 1549–1559.

[35] Jing, L. Y.; Sun, J. W.; Sun, C. Y.; Wu, D.; Lian, G.; Cui, D. L.; Wang, Q. L.; Yu, H. H. $MoS_2$-intercalated carbon hetero-layers bonded on graphene as electrode materials for enhanced sodium/potassium ion storage. *Nano Res.* **2023**, *16*, 473–480.

[36] Zhang, Y. F.; Meng, N.; Babar, A. A.; Wang, X. F.; Yu, J. Y.; Ding, B. Multi-bioinspired and multistructural integrated patterned nanofibrous surface for spontaneous and efficient fog collection. *Nano Lett.* **2021**, *21*, 7806–7814.

[37] Wu, C. H.; Ou, J. Z.; He, F. Y.; Ding, J. F.; Luo, W.; Wu, M. H.; Zhang, H. J. Three-dimensional $MoS_2$/carbon sandwiched architecture for boosted lithium storage capability. *Nano Energy* **2019**, *65*, 104061.

[38] Wang, L. L.; Zhang, Y. X.; Gu, C.; Yu, H. X.; Zhuang, Y. L.; Zhuang, Z. C. Diverse atomic structure configurations of metal-doped transition metal dichalcogenides for enhancing hydrogen evolution. *Nano Res.* **2024**, *17*, 3586–3602.

[39] Xia, J. K.; Xu, J. W.; Yu, B.; Liang, X.; Qiu, Z.; Li, H.; Feng, H. J.; Li, Y. F.; Cai, Y. J.; Wei, H. Y. et al. A metal-sulfur-carbon catalyst mimicking the two-component architecture of nitrogenase. *Angew. Chem., Int. Ed.* **2024**, *63*, e202412740.

[40] Zhang, N. N.; Gao, X. Y.; Guan, H. R.; Sun, S. M.; Liu, J. M.; Shao, Z. T.; Gao, Q. Y.; Zhang, Y.; Sun, R. Y.; Yang, G. et al. Three-dimensional porous $In_2O_3$ arrays for self-powered transparent solar-blind photodetectors with high responsivity and excellent spectral selectivity. *Nano Res.* **2024**, *17*, 4471–4477.

[41] Shan, T. T.; Xin, S.; You, Y.; Cong, H. P.; Yu, S. H.; Manthiram, A. Combining nitrogen-doped graphene sheets and $MoS_2$: A unique film-foam-film structure for enhanced lithium storage. *Angew. Chem., Int. Ed.* **2016**, *55*, 12783–12788.

[42] Yue, L.; Zhang, W. H.; Zhang, W. D.; Zhang, Q. F.; Guan, R. F.; Hou, G. H.; Xu, N. One-step solvothermal process of $In_2O_3$/C nanosheet composite with double phases as high-performance lithium-ion battery anode. *Electrochim. Acta.* **2015**, *160*, 123–130.

[43] Liu, H. P.; Lei, W.; Tong, Z. M.; Guan, K. K.; Jia, Q. L.; Zhang, S. W.; Zhang, H. J. Enhanced diffusion kinetics of Li ions in double-shell hollow carbon fibers. *ACS Appl. Mater. Interfaces* **2021**, *13*, 24604–24614.

[44] Tan, C. L.; Zhang, H. Two-dimensional transition metal dichalcogenide nanosheet-based composites. *Chem. Soc. Rev.* **2015**, *44*, 2713–2731.

[45] Sun, Y. F.; Wang, Y. X.; Chen, J. Y. C.; Fujisawa, K.; Holder, C. F.; Miller, J. T.; Crespi, V. H.; Terrones, M.; Schaak, R. E. Interface-mediated noble metal deposition on transition metal dichalcogenide nanostructures. *Nat. Chem.* **2020**, *12*, 284–293.

[46] Wu, X. Y.; Wu, H. Y.; Xie, B.; Wang, R.; Wang, J. M.; Wang, D. G.; Shi, Q. F.; Diao, G. W.; Chen, M. Atomic welded dual-wall hollow nanospheres for three-in-one hybrid storage mechanism of alkali metal ion batteries. *ACS Nano* **2021**, *15*, 14125–14136.

[47] Zhao, X. W.; Liu, Z. C.; Xiao, W. Y.; Huang, H. Y.; Zhang, L. H.; Cheng, Y. H.; Zhang, J. Y. Low crystalline $MoS_2$ nanotubes from $MoS_2$ nanomasks for lithium ion battery applications. *ACS Appl. Nano Mater.* **2020**, *3*, 7580–7586.

[48] Rao, Y.; Wang, J.; Liang, P. H.; Zheng, H. J.; Wu, M.; Chen, J. T.; Shi, F.; Yan, K.; Liu, J. S.; Bian, K. et al. Heterostructured $WS_2$/$MoS_2$@carbon hollow microspheres anchored on graphene for high-performance Li/Na storage. *Chem. Eng. J.* **2022**, *443*, 136080.

[49] Zeng, T. B.; Feng, D.; Liu, Q.; Zhou, R. Y. Confining nano-GeP in nitrogenous hollow carbon fibers toward flexible and high-performance lithium-ion batteries. *ACS Appl. Mater. Interfaces* **2021**, *13*, 32978–32988.

[50] Yan, L.; Zhao, F.; Wang, J.; Zu, Y.; Gu, Z. J.; Zhao, Y. L. A safe-by-design strategy towards safer nanomaterials in nanomedicines. *Adv. Mater.* **2019**, *31*, 1805391.